Received: 23 June 2019 | Revised: 8 August 2019 | Accepted: 30 August 2019

DOI: 10.1111/ffe.13134

INVITED REVIEW ARTICLE

WILEY FFEMS Fatigue & Fracture of Engineering Materials & Structures

Stress–strain curves of metallic materials and post-necking strain hardening characterization: A review

Shengwen Tu[1] | **Xiaobo Ren**[2] | **Jianying He**[1] | **Zhiliang Zhang**[1]

[1] Department of Structural Engineering, Norwegian University of Science and Technology (NTNU), Trondheim 7491, Norway

[2] SINTEF Industry, Trondheim 7465, Norway

Correspondence
Zhiliang Zhang, Department of Structural Engineering, Norwegian University of Science and Technology (NTNU), Trondheim 7491, Norway.
Email: zhiliang.zhang@ntnu.no

Funding information
Chinese Scholarship Council; Research Council of Norway, Grant/Award Number: 228513/E30

Abstract

For metallic materials, standard uniaxial tensile tests with round bar specimens or flat specimens only provide accurate equivalent stress–strain curve before diffuse necking. However, for numerical modelling of problems where very large strains occur, such as plastic forming and ductile damage and fracture, understanding the post-necking strain hardening behaviour is necessary. Also, welding is a highly complex metallurgical process, and therefore, weldments are susceptible to material discontinuities, flaws, and residual stresses. It becomes even more important to characterize the equivalent stress–strain curve in large strains of each material zone in weldments properly for structural integrity assessment. The aim of this paper is to provide a state-of-the-art review on quasi-static standard tensile test for stress–strain curves measurement of metallic materials. Meanwhile, methods available in literature for characterization of the equivalent stress–strain curve in the post-necking regime are introduced. Novel methods with axisymmetric notched round bar specimens for accurately capturing the equivalent stress–strain curve of each material zone in weldment are presented as well. Advantages and limitations of these methods are briefly discussed.

KEYWORDS

Bridgman correction, diffuse necking, equivalent stress–strain curve, post-necking strain hardening, tensile test

1 | INTRODUCTION

Numerical analyses are frequently utilized to model sheet metal operations, such as hydroforming,[1,2] deep drawing,[3-6] and stamping,[7-9] to reduce trial-and-error iterations in the design stage. Structural integrity assessment with finite element method in elastoplastic domain requires the equivalent stress–strain curve in large strain range, especially for ductile damage and fracture modelling with cracked specimens, [10-17] of which the crack tip exhibits very complex stress and strain gradient. For such kinds of engineering processes, large strain develops and even exceeds the uniform elongation measured from standard tensile test. In order to provide reliable predictions numerically in analyses that involve large strains, accurate identification of the equivalent stress–strain relationship in the post-necking regime is important. Materials' equivalent stress–strain curves are usually measured from

standard quasi-static uniaxial tensile test with smooth round bar specimen for thick plates and rectangular cross-section specimen (referred as "flat specimen" hereafter) for thin sheet metals. For conventional strain measurement techniques used in uniaxial tensile test, such as strain gauge and extensometers, only the data before diffuse necking is valid and can be used directly. After the onset of diffuse necking, deformation is localized in the necking zone alongside with the development of triaxial stress state. Due to the non-uniform deformation on the testing coupon, characterization of the minimum cross-section area is a difficult task, especially for the testing coupons with initial rectangular cross section. For inhomogeneous sections, such as weldment, it is even more challenging to accurately evaluate the equivalent stress–strain curve. The reasons are that the microstructures of weldments are very complex and the fracture location is practically unpredictable on the cross-weld tensile specimens. As a result, the load-elongation curves from cross-weld specimens are not representative and cannot be used for mechanical applications directly, for example, the structural integrity assessment. These issues mentioned above lead to the challenges for determining equivalent stress–strain curve in the post-necking regime.

To cope with these challenges and identify post-necking hardening behaviour, many methods have been proposed in the past decades. These methods, in general, can be classified into three groups. The first group is the analytic solutions derived with smooth round bar specimens based on some assumptions. These methods provide approximate stress distribution in the neck, as functions of neck geometry parameters: the neck curvature radius and the neck radius.[18-20] The best known is the so-called Bridgman method.[18] The second group is the experimental-numerical iterative approaches.[21-25] For such methods, some quantities, such as load-displacement curve and surface strain distribution, measured from experiments are compared with those from numerical modelling. Accurate equivalent stress–strain curve can be obtained by iteratively optimizing the post-necking hardening behaviour, until good agreement between experimental measured quantities and numerical modelled results is achieved. The third group is the so-called inverse methods.[26-28] A series of correction formulae was proposed to convert the true stress–strain curves to the equivalent stress–strain curves. These formulae were derived numerically by studying the relationship between the input equivalent stress–strain curve and the average axial stress-equivalent strain curve from numerical tensile test. As mentioned above, numerous methods have been proposed for the identification of the post-necking strain hardening behaviour of metallic materials. All these methods, if capable of delivering reasonable degrees of approximation, are worth promoting, as each method can be the preferred one among others for each member of the scientific community.

This work presents a review of the standard uniaxial tensile test and the proposed methods for post-necking strain hardening identification. In the following, the standard quasi-static uniaxial tensile test is briefly introduced in Section 2. Some basic definitions involved in are annotated and presented. Next, methods for post-necking strain hardening characterization are presented, classified in the same way above. Application of these methods and their accuracy are also discussed. Finally, the major conclusions can be found in Section 4.

2 | STANDARD QUASI-STATIC UNIAXIAL TENSILE TEST AND BASIC DEFINITIONS

The uniaxial tensile test for metallic materials has been standardized for a long time, and many national/international guidelines or protocols are developed, such as ASTM E8/E8M-16a,[29] ISO 6892-1,[30] 6892-2,[31] and JIS Z2241.[32] From a standard tensile test, material mechanical properties, including Young modulus (E), yield/tensile strength (σ_0,σ_u), and uniform elongation (ε_u) can be obtained. In this section, the standard quasi-static uniaxial tensile test is briefly introduced and some basic definitions are presented.

2.1 | Standard quasi-static uniaxial tensile test

The uniaxial tensile test is frequently performed in mill test to guarantee the predefined products performance and in the laboratory to provide basic and important material constitutive relationships for the structural integrity assessment. Small coupons are usually machined from structural sections in the rolling direction, transversal direction, or the normal direction. For thick plates, smooth round bar specimens can be considered, while for very thin plates, flat specimen is more popular. A testing coupon is schematically shown in Figure 1. Before performing the test, some initial geometry parameters should be measured. These parameters include the gauge length (L_0), the cross-section radius (d_0=2r_0) for smooth round bar coupons, or specimen width (W_0) and

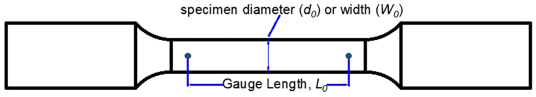

FIGURE 1 Schematic illustration of a tensile testing coupon [Colour figure can be viewed at wileyonlinelibrary.com]

thickness (t_0) for flat specimens. The uniaxial tensile test is performed on an universal testing machine, usually in displacement control. The quantities measured directly from the test are the axial load (P) obtained from the load cell and the engineering strain (ε_e) measured by the extensometer or the strain field with the digital image correlation (DIC) method. During the tensile test, the coupon undergoes uniform deformation, followed by diffuse necking and the ensuing fully fracture. Several definitions of stress–strain relationships can be obtained after performing the standard uniaxial tensile test.

2.2 | Engineering stress–strain curve

The engineering stress–strain curve, also known as the nominal stress–strain curve, can be easily obtained from the conventional uniaxial tensile test. The engineering strain is defined by the uniaxial deformation relative to the initial gauge length L_0:

$$\varepsilon_e = \frac{L - L_0}{L_0} = \frac{\Delta L}{L_0} \tag{1}$$

where L is the deformed gauge length in tensile direction. The engineering stress σ_e is defined by dividing the load by the initial cross-section area A_0:

$$\sigma_e = \frac{P}{A_0} \tag{2}$$

By plotting the engineering stress against the engineering strain, one can conveniently construct the engineering stress–strain curve, as schematically shown in Figure 2. In general, the engineering stress–strain curve can be divided into four regimes. At the very beginning, the deformation is very small and the specimen is elastic. Correspondingly, a linear relationship exists between the engineering stress σ_e and the engineering strain ε_e. The engineering stress increases linearly with the increase of the engineering strain in the elastic regime and terminates when the specimen enters into plastic domain. The second regime in Figure 2 is known as yielding, which takes place when the specimen just enter into plastic domain. In this stage, the yield stress can be defined by the offset method or the extension-under-load (EUL) method for some discontinuous yielding materials.[29] The offset method is to draw a linear line parallel to the elastic part of the engineering stress–strain curve and then offset to a specified value of extension, usually 0.2%. The corresponding engineering stress of the intersection constructed by the offset line and the engineering stress–strain curve is the yield stress and expressed as $\sigma_{0.2}$, as shown in Figure 2. For the EUL method, the yield stress is determined by the engineering stress at a specified extension, for example, 0.5%. Correspondingly, the yield stress is expressed as $\sigma_{0.5}$. For materials that exhibits discontinuous yielding, both the upper and lower stress should be disclosed according to those recommended guidelines. It should be noted that both the elastic part and the yielding happen in the very early stage in the whole deformation history. After yielding, the engineering stress increases with the increase of the engineering strain. This part, marked by green background in Figure 2, is known as strain hardening. After reaching the maximum engineering stress, plastic instability and flow localization will occur just after the maximum load and the so-called diffuse necking starts. The maximum engineering stress is known as the ultimate tensile stress σ_u, and the corresponding engineering strain is called the uniform elongation ε_u. After the onset of diffuse necking, the deformation is localized in the necking zone. Necking in a uniaxial cylindrical tensile specimen is axisymmetric. For flat specimens, diffuse necking may terminate in fracture. But usually after the onset of the diffuse neck, the deformation continues under the falling load until the development of a localized neck, which leads ultimately to ductile fracture. The localized necking is a narrow band with about equal to the sheet thickness and inclined at an angle to the specimen axis, across the width of the specimen. A sudden drop of engineering stress can be observed when the specimen breaks apart. In this stage, the data obtained from the extensometer is no longer valid, since the uniaxial deformation assumption does not stand.

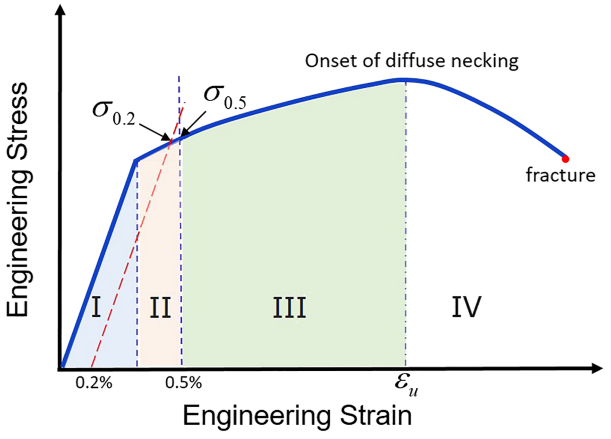

FIGURE 2 Engineering stress-engineering strain curves from uniaxial tensile test [Colour figure can be viewed at wileyonlinelibrary.com]

2.3 | True stress–strain curve

The engineering stress and the engineering strain are defined in terms of the initial specimen geometric

parameters, without considering the cross-section change when large strain occurs. Therefore, it is more practical to define the strain increment with respect to the current gauge length L as Equation (3)

$$d\varepsilon_t = \frac{dL}{L} \tag{3}$$

where ε_t is the true strain. Integrating Equation (3), one can have

$$\varepsilon_t = \int_{L_0}^{L} \frac{dL}{L} = \ln\left(\frac{L}{L_0}\right) = \ln\left(\frac{L_0 + \Delta L}{L_0}\right) = \ln(1 + \varepsilon_e) \tag{4}$$

ε_t is also know as the logarithmic strain. Correspondingly, the true stress is defined as

$$\sigma_t = \frac{P}{A} \tag{5}$$

where A is the current cross-section area. Assuming volume constancy, namely,

$$A_0 L_0 = AL \tag{6}$$

$$\sigma_t = \frac{P}{A} = \frac{PL}{A_0 L_0} = \sigma_e(1 + \varepsilon_e) \tag{7}$$

According to Equations (4) and (7), the engineering stress and the engineering strain measured from the tensile test can be converted to the true stress and the true strain. Figure 3 schematically shows the difference of true stress–strain curve and engineering stress–strain curve from uniaxial tensile tests.

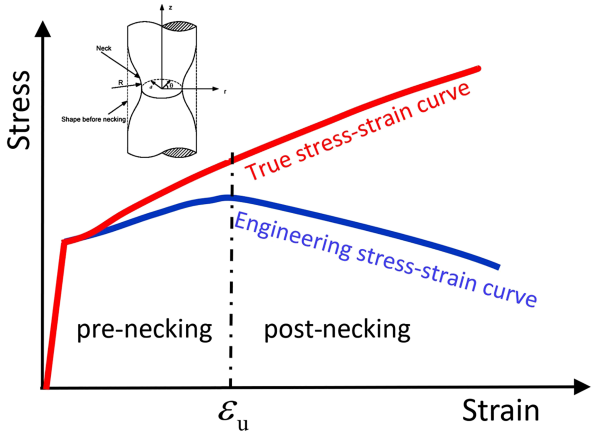

FIGURE 3 Schematically illustration of the engineering stress–strain curve and true stress–strain curve from uniaxial tensile test. The true stress–strain curve after diffuse necking can be obtained by experimental measurement or extrapolation with mathematical models [Colour figure can be viewed at wileyonlinelibrary.com]

Inversely, the engineering stress can be expressed as

$$\sigma_e = \sigma_t \exp(-\varepsilon_t) \tag{8}$$

The incremental change of the engineering stress can be written as

$$d\sigma_e = (d\sigma_t - \sigma_t d\varepsilon_t)exp(-\varepsilon_t) \tag{9}$$

When the engineering stress reaches its maximum value, we have $d\sigma_e$=0 and dP=0. Just after the maximum load, the so-called diffuse necking sets in. Then, the criterion for the onset of diffuse necking (also known as Considére criterion[33]) determined from the true stress–strain curve can be expressed as

$$\sigma_{t,necking} = \frac{d\sigma_t}{d\varepsilon_t}\Big|_{\varepsilon_t = \varepsilon_{t,necking}} \tag{10}$$

where $\sigma_{t,necking}$ and $\varepsilon_{t,necking}$ are the true stress and true strain at diffuse necking, respectively. After performing the tensile test, the fracture surface area is measured and used to calculate the fracture strain ε_f.

$$\varepsilon_f = \ln\left(\frac{A_0}{A_f}\right) \tag{11}$$

where A_f is the fracture surface area. ε_f is also the parameter to represent materials' ductility, which has been proved to be sensitive to the hydrostatic stress.[34-36]

For simplification, some mathematical models have been proposed to fit the true stress–strain curves for theoretical or analytical solutions. Occasionally, these models are used to extrapolate the true stress after diffuse necking. In the following, classical mathematical models, including the linear model, the Hollomon model, and the Ramberg-Osgood model, will be briefly introduced.

1. Linear model
   The linear model is the simplest one with the assumption that the true stress-true strain curve is linear after yielding. The linear model can be written as

   $$\sigma_t = a_1 \varepsilon_t + b_1 \tag{12}$$

   where a_1 and b_1 are the unknown coefficients, which can be obtained with Equations (4), (7), and (10).
2. Hollomon model
   The Hollomon model is a power law relating the true strain to the true stress, proposed by Hollomom.[37] The Hollomon model has the form:

   $$\sigma_t = K_1 \varepsilon_t^{n_1} \tag{13}$$

   where K_1 and n_1 are the strength coefficient and the strain hardening exponent, respectively. These two parameters are obtained by fitting the data of the true

stress and true strain from yielding to diffuse necking. According to Equation (10), we have $\varepsilon_{t,necking}=n_1$. It means that for the Hollomon model, diffuse necking occurs at the equivalent strain, of which the value is exactly equal to n_1. The linear model and the Hollomon are frequently used alone or together piecewisely to represent the materials' true stress–strain curve, for different metallic materials, such as steel, copper, and alloys.[38]

3. Ramberg-Osgood model
The Ramberg-Osgood model is also used to describe the non-linear relationship between the true stress and the true strain after yielding.[39] The Ramberg-Osgood model can be written as

$$\frac{\varepsilon_t}{\varepsilon_y}=\frac{\sigma_t}{\sigma_y}+\alpha\left(\frac{\sigma_t}{\sigma_y}\right)^{n_2} \tag{14}$$

where σ_y and ε_y are the yield stress and the elastic strain at yielding, which are determined by the offset method mentioned above. α is a material parameter, and $\alpha(\sigma_y/E)$ can be seen as a yield offset. n_2 is the hardening parameter that is derived by fitting the date from yielding to diffuse necking with Equation (14).

2.3.1 | Post-necking true stress–strain curve characterization

Before diffuse necking, deformation on the test coupons is uniform. The true stress–strain curve can be easily obtained. However, the diffuse necking-induced triaxial stress state in the necking zone results in strong challenges for the characterization of true stress–strain relationships. Attentions have been paid to identify the relationship between the true stress and true strain in the post-necking domain, and several methods were proposed. These methods can be divided into two groups. The first group is the extrapolation of true stress by some mathematical formulae, such as the linear model and the Hollomon model. However, the extrapolation method is not trustful due to the complex stress state in the necking zone. The second group, which will be introduced next, is to characterize the minimum cross-section area (smooth round bar specimens or flat specimens) after diffuse necking.

1. Smooth round bar specimen
For the smooth round bar specimen, it is assumed that the specimen geometry is always axisymmetric during the whole range of tensile deformation. Therefore, the true strain is characterized by the contraction of the specimen minimum cross-section area:

$$\varepsilon_t=\ln\left(\frac{A_0}{A}\right)=2\ln\left(\frac{a_0}{a}\right) \tag{15}$$

where a_0 and a are the specimen initial cross-section radius and current minimum cross-section radius, respectively. a can be measured with a linear variable displacement transducer or the so-called edge tracing method.[40,41] The true stress after diffuse necking can also be obtained by Equation (5).

2. Axisymmetric notched bar specimen
It is important to know the mechanical behaviour of each material zone in weldments for structural integrity assessment. However, for cross-weld tensile specimens, the load and elongation measured from an uniaxial tensile test cannot be used for numerical analysis, due to the inhomogeneous material structure and unpredictable fracture location. To cope with this challenge, Zhang et al proposed to use axisymmetric notched bar specimen for true stress–strain curve characterization in large range of strain (Figure 4).[42] By introducing a notch with curvature radius of R_0 in the target material zone on a smooth round bar specimen, the deformation is forced to localize in the notch. Similar to the smooth round bar specimens, the true stress and true strain are characterized by Equations (5) and (15). Due to the introduction of the notch, stress concentration occurs, and as a results, the true stress from a notched specimen ($\sigma_t^{Notched}$) calculated by Equation (5) differs significantly from the true stress of a smooth round bar specimen (σ_t^{Smooth}). The true stress–strain curve obtained from the axisymmetric notched specimen can be converted to the true stress–strain curve from a smooth round bar specimen by a G factor[42]:

$$\sigma_t^{Smooth}(\varepsilon_t)=\sigma_t^{Notched}(\varepsilon_t)/G \tag{16}$$

The G factor is expressed by Equation (17):

$$G=\left[1.007+0.18777\left(\frac{D_0}{R_0}\right)-0.01313\left(\frac{D_0}{R_0}\right)^2\right]\times(1.053-0.53\varepsilon_{p_{max}}) \tag{17}$$

where $\varepsilon_{p_{max}}$ is the true strain corresponding to the maximum tensile load, which is approximately equal to the true strain at diffuse necking, ε_u. As can be seen, G is a function of the notch geometry parameters a_0/R_0 and the material hardening properties $\varepsilon_{p_{max}}$. Further investigation indicates that when the zone

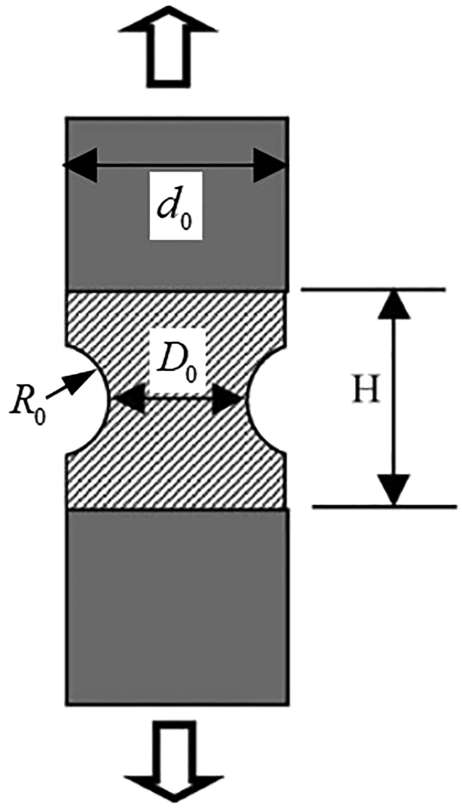

FIGURE 4 Notched cross-weld tensile specimen proposed by Zhang et al for true stress–strain curve measurement of each material zone in weldment.[42] The notched region marked by shadow can be under-match, even-match or over-match with the rest parts

length H is larger than D_0, the true stress–strain curve from bimaterial specimen is the same with the one from homogeneous material. This observation shows great potential for the application of the axisymmetric notched bar specimen to measure true stress–strain curve of each individual material zone of inhomogeneous materials.

3. Flat specimen

For thick sections, smooth round bar specimen can be machined to measure the true stress–strain curve after diffuse necking, while flat specimens are more suitable for thin sections. The problem is that the instantaneous minimum cross-section area of a necked flat specimen is difficult to measure accurately. For this purpose, Zhang et al proposed an inverse method to evaluate the minimum cross-section reduction after necking with finite element analysis.[26] In Zhang's method, the total area reduction ratio of a rectangular tensile specimen at the minimum cross section can be separated into a proportional part calculated from the thickness reduction and another nonproportional part due to shape change:

$$\frac{\Delta A}{A_0} = \frac{\Delta A_P}{A_0} - \frac{\Delta A_S}{A_0} \tag{18}$$

where the first part in the right-hand side of Equation (18) is the same as a round specimen and can be written as a function of the minimum cross-section thickness reduction ($\Delta t/t_0$):

$$\frac{\Delta A_P}{A_0} = 2\left(\frac{\Delta t}{t_0}\right) - \left(\frac{\Delta t}{t_0}\right)^2 \tag{19}$$

The nonproportional part is expressed as

$$\frac{\Delta A_S}{A_0} = f_s(S) f_t\left(\frac{\Delta t}{t_0} - \left(\frac{\Delta t}{t_0}\right)_{P_{max}}\right) f_m\left(\frac{\Delta t}{t_0}\right)_{P_{max}} \tag{20}$$

where P_{max} is the maximum tensile load. The first part in Equation (20) is a function of the specimen aspect ratio S, which is a specimen geometry parameter.

$$f_s(S) = 0.1686 + 0.6\ln(S) \tag{21}$$

The second and third parts in Equation (20) depend on the total cross-section thickness reduction and thickness reduction at the maximum tensile load. Since diffuse necking occurs just after P_{max}, therefore, $(\Delta t/t_0)_{P_{max}}$ represents material hardening effect on the nonproportion area reduction. The second and third part in Equation (20) are expressed as

$$f_t(x) = c_0 + c_1 x + c_2 x^2 + c_3 x^3 + c_4 x^4 \tag{22}$$

where $x = (\Delta t/t_0) - (\Delta t/t_0)_{P_{max}}$ and c_0=−0.03069, c_1=1.09016, c_2=11.1512, c_3=−25.1, and c_4=14.8718 are constants.

$$f_m = 0.2845 - 0.956\left(\frac{\Delta t}{t_0}\right)_{P_{max}} \tag{23}$$

With Equations (19) and (20), the post-necking minimum cross-section area can be determined when the thickness reduction is measured accurately, so does the true stress–strain curve. Meanwhile, this method has also been generalized to anisotropic materials.[27]

2.4 | Equivalent stress–strain curve

For the isotropic, homogeneous materials, the stress state of a material point is very complex in 3D with six

independent stress components. The stress state is usually represented by a so-called equivalent stress, to determine whether the yielding take place or not. The so-called von Mises equivalent stress is widely used in engineering application. The von Mises equivalent stress can be calculated as

$$\sigma_{eq} = \sqrt{\frac{1}{2}\left[(\sigma_{11}-\sigma_{22})^2 + (\sigma_{22}-\sigma_{33})^2 + (\sigma_{33}-\sigma_{11})^2 + 6(\sigma_{23}^2 + \sigma_{31}^2 + \sigma_{12}^2)\right]} \tag{24}$$

where σ_{11}, σ_{22}, σ_{33}, σ_{12}, σ_{13}, and σ_{23} are the true stress components. Correspondingly, the equivalent strain has the form

$$\varepsilon_{eq} = \frac{2}{3}\sqrt{\frac{(\varepsilon_{11}-\varepsilon_{22})^2 + (\varepsilon_{22}-\varepsilon_{33})^2 + (\varepsilon_{11}-\varepsilon_{33})^2 + 6(\varepsilon_{12}^2 + \varepsilon_{13}^2 + \varepsilon_{23}^2)}{2}} \tag{25}$$

where ε_{11}, ε_{22}, ε_{33}, ε_{12}, ε_{13}, and ε_{23} are the true strain components. One can get the equivalent stress–strain curve by plotting the von Mises equivalent stress against the equivalent strain. For uniaxial tensile test before necking, the stress components are zero, except the one in the tensile direction, denoted as σ_{11}. In this case, the tensile stress equals to the von Mises equivalent stress. The shear strain components (ε_{12}, ε_{13}, and ε_{23}) are zeros before necking in the uniaxial tensile test. The strain components in thickness (radial) and width (circumferential) directions are calculated:

$$\varepsilon_{22} = \varepsilon_{33} = -\frac{1}{2}\varepsilon_{11} \tag{26}$$

Inserting Equation (26) into Equation (25), the equivalent strain can be obtained and equals to ε_{11}. Therefore, for the uniaxial tensile test, the true stress–strain curve obtained before diffuse necking is also the material's equivalent stress–strain curve. After the onset of diffuse necking, the uniaxial deformation assumption is no longer valid. The true stress calculated by Equation (5) differs from the equivalent stress calculated by Equation (24), due to the necking-induced triaxial stress state. The equivalent stress–strain curve after diffuse necking is the main concern in this work and will be discussed in detail in Section 3.

2.5 | Flow stress–strain curve

When plasticity takes place in a material, the instantaneous stress required to continue plastically deforming the material is called the flow stress. The equivalent strain can be additively decomposed into elastic and plastic parts:

$$\varepsilon_{eq} = \bar{\varepsilon}^e + \bar{\varepsilon}^p \tag{27}$$

where $\bar{\varepsilon}^e = \sigma_{eq}/E$ is the elastic strain component and E is the Young modulus. $\bar{\varepsilon}^p$ is the equivalent plastic strain. The flow stress–strain curve can be constructed by plotting the equivalent stress against the corresponding equivalent plastic strain. The flow stress–strain curve is the direct input data for numerical modelling in some commercial FE software, for example, Abaqus. Some mathematical models are proposed to fit the flow stress–strain curve converted from the experimental measured equivalent stress–strain curve. Some of these models are frequently used in numerical modelling.

1. Power-law model
   The power-law model has a very simple form:
   $$\sigma_{eq} = \sigma_0\left(\frac{1+\bar{\varepsilon}^p}{\varepsilon_0}\right)^{n_3} \tag{28}$$
   where σ_0 and ε_0 are the yield stress and the yield strain, determined as the elastic termination point on the equivalent stress–strain curve, $\varepsilon_0=\sigma_0/E$. n_3 is the strain hardening exponent. The higher n_2 is, the higher the strain hardening capacity the material displays. When $n_2=0$, the flow stress is always equal to the yield stress and independent of the equivalent plastic strain. In this case, the material is also referred as the perfectly plastic material.
2. Swift model
   The Swift model is in the similar form as Hollomon model, with another parameter ε_0:
   $$\sigma_{eq} = K_2\left(\varepsilon_{0,Swift} + \bar{\varepsilon}^p\right)^{n_4} \tag{29}$$
   where K_2, $\varepsilon_{0,Swift}$, and n_4 are adjustable parameters determined by fitting the experimental data. The Swift model can be achieved by moving the stress axis of the Hollomon model along the positive strain axis through a distance of $\varepsilon_{0,Swift}$. Therefore, the Swift model is more suitable when prior cold work is involved, with $\varepsilon_{0,Swift}$ representing the amount of prestrain.
3. Voce model
   In a tensile test, the flow stress of some materials may display non-linearly with the increment of the equivalent plastic strain first, saturated into a constant value with further plastic deformation. This kind of materials can be fitted by the Voce model:
   $$\sigma_{eq} = k_0 + Q(1 - exp(-\beta\bar{\varepsilon}^p)) \tag{30}$$
   where k_0, Q, and β are fitted parameters.

In addition to the models introduced above, other models, such as the Ludwigson model and Kock-Mecking-Estrin model, are proposed for specific materials. Meanwhile, a weighting factor can be introduced to combine one model with two pairs of fitting parameters or two different models to better represent the material's flow stress–strain curve.[41]

3 | METHODS FOR POST-NECKING STRAIN HARDENING IDENTIFICATION

As introduced in Section 2, the true stress–strain curve or the flow stress–strain curve obtained from the uniaxial tensile test can be used as input data for numerical modelling. However, only the data in the pre-necking domain is valid. Though the flow stress can be extrapolated by the fitted mathematical models of the true stress–strain curve or the flow stress–strain curve, one can not guarantee the accuracy of the predictions. Figure 5 schematically show the difference between the true stress (extrapolated) and the equivalent stress after diffuse necking. For numerical modelling of large strains problems, such as the analysis of plastic forming and modelling of ductile fracture, it is very necessary to understand the post-necking strain hardening behaviour beforehand to accurately capture the desired results. In the next context, methods for post-necking strain hardening identification will be introduced. If not stated else, the target stress–strain curve will be the equivalent one, since the flow stress–strain curve can be conveniently converted by Equation (27).

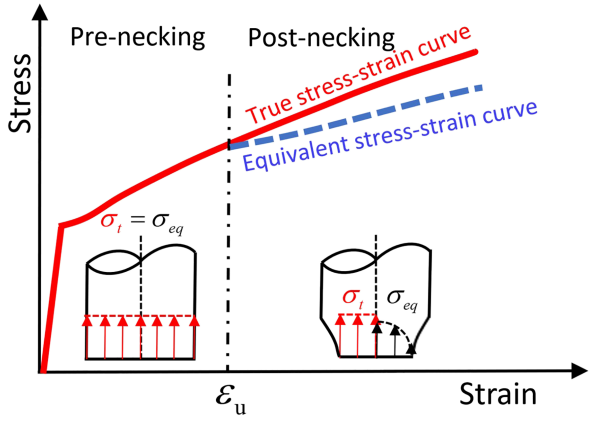

FIGURE 5 Difference between the true stress and the equivalent stress after diffuse necking. The true stress and equivalent stress distribution at the minimum cross-section before and after diffuse necking are also schematically displayed [Colour figure can be viewed at wileyonlinelibrary.com]

3.1 | Analytical solutions with smooth round bar specimen

Considering the importance of the hardening behaviour after diffuse necking, many pioneering efforts have been paid to retrieve the accurate post-necking constitutive information. Correcting the true stress back to the equivalent stress in the post-necking regime with smooth round bar specimens has a very long history, and several analytical approaches have been proposed. The most popular correction formula was proposed by Bridgman.[18] Figure 6 shows a necked geometry of a smooth round bar tensile sample schematically. For the derivation of the Bridgman correction formula, there are two assumptions:

- In a certain surrounding of the neck, the value of the strains and equivalent stress, σ_{eq}, is constant (this region is shown in the Figure 6A).
- In the surrounding of the minimal section, the shape of the transverse trajectories of the principal stress are arcs that are orthogonal to the longitudinal trajectories; see in Figure 6B.

Due to the axial symmetry of the smooth round bar specimen, the equilibrium equation in the minimum cross section can be written as

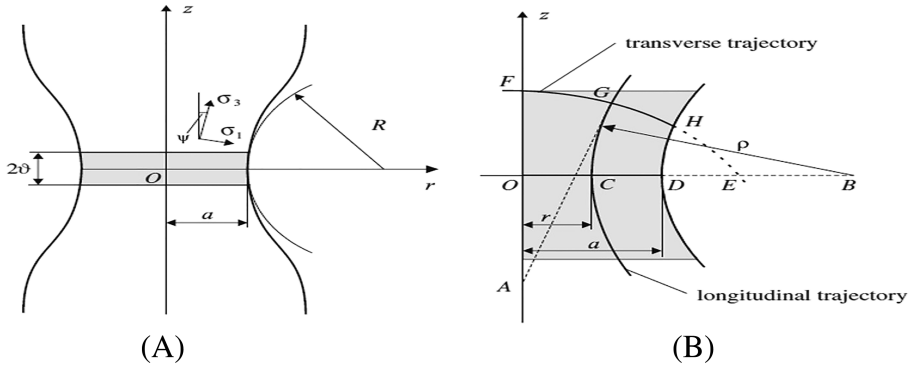

FIGURE 6 A, Neck geometry in a tension sample and B, principal stress trajectories in the meridian surface[43]

$$\frac{\partial \sigma_{rr}}{\partial r}+\frac{\partial \tau_{rz}}{\partial z}+\frac{\sigma_{rr}-\sigma_{\theta\theta}}{r}=0 \tag{31}$$

where σ_{rr} and $\sigma_{\theta\theta}$ are stresses in r and θ direction. τ_{rz} is the shear stress. According to the condition of volume conservation in plastic regime and the assumption that strains are constant in the minimum cross section, the radial displacement can be expressed as $u_r{=}\varepsilon_{rr}{\cdot}r$. u_r and ε_{rr} are displacement and strain in radial direction, respectively. Therefore, in the minimal section, the circumferential strain is equal to the radial strain and $\sigma_{rr}=\sigma_{\theta\theta}$, since $\varepsilon_{\theta\theta}{=}u_r/r{=}\varepsilon_{rr}$. Then, the third term in Equation (31) vanishes. According to the von Mises yielding criteria, we have

$$\sigma_{eq}=\sigma_{zz}-\sigma_{rr} \tag{32}$$

Taking into consideration of the relation Equation (32) and the first assumption, Equation (31) takes the following form:

$$\frac{\partial \sigma_{zz}}{\partial r}+\frac{\partial \tau_{rz}}{\partial z}=0 \quad when \quad z=0,\ 0<r<a \tag{33}$$

σ_{zz} is the stress in tensile direction. In Figure 6A, ψ is very small, and τ_{rz} can be expressed as

$$\sigma_{rr}\approx\sigma_1 \quad \sigma_{zz}\approx\sigma_3, \quad \tau_{rz}=(\sigma_3-\sigma_1)\psi=\sigma_{eq}\psi \tag{34}$$

where σ_1 and σ_3 are the principle stresses. The second term in Equation (33) can be written as

$$\begin{aligned}\left(\frac{\partial \tau_{rz}}{\partial z}\right)_{z=0} &= \left(\frac{\partial(\sigma_{eq}\psi)}{\partial z}\right)_{z=0}=\sigma_{eq}\left(\frac{\partial \psi}{\partial z}\right)_{z=0}\\ &+\psi_0\left(\frac{\partial \sigma_{eq}}{\partial z}\right)_{z=0_0}=\sigma_{eq}\left(\frac{\partial \psi}{\partial z}\right)_{z=0}\end{aligned} \tag{35}$$

Since the angle ψ is very small, we obtain

$$\psi(r,z)\approx tan\psi(r,z)=f_C^{'}(z) \tag{36}$$

where $f_C(z)$ is the appropriate longitudinal trajectory passing through point C on the OB axis (Figure 6B). Calculating the derivative from Equation (36),

$$\left(\frac{\partial \psi}{\partial z}\right)=f^{''}(z) \tag{37}$$

The curvature of the principal stress trajectory σ_3 can be calculated as

$$\frac{1}{\rho}=\frac{\left|f^{''}(z)\right|}{(1+f^{'}(z)^2)^{(3/2)}} \tag{38}$$

Inserting Equations (36) to 38 into Equation (35), in the plane $z{=}0$, $\psi{=}0$, we obtain

$$\sigma_{eq}\left(\frac{\partial \psi}{\partial z}\right)_{z=0}=\sigma_{eq}\left[\frac{(1+\psi^2(r,z))^{3/2}}{\rho}\right]=\frac{\sigma_{eq}}{\rho} \tag{39}$$

In Figure 6B from the geometric relationship, we have

$$\begin{aligned}\rho^2=BG^2&=AB^2-AE^2=OB^2-OE^2\\&=(r+\rho)^2-OE^2\end{aligned} \tag{40}$$

Equation (40) is valid for any point G on the circle FGH, including the point H. Then we have

$$r^2+2r\rho=a^2+2aR=OE^2 \tag{41}$$

$$\rho=\frac{a^2+2aR-r^2}{2r} \tag{42}$$

Inserting Equations (39) and (42) to Equation (33) and solve the equation, we obtain

$$\begin{aligned}\sigma_{zz} &= \sigma_{eq}\left[1+ln(1+\frac{a^2-r^2}{2aR})\right]\\ \sigma_{rr} &= \sigma_{\theta\theta}=\sigma_{eq}{\cdot}ln(1+\frac{a^2-r^2}{2aR})\end{aligned} \tag{43}$$

where R and a are the necking curvature radius and the minimum cross-section radius, respectively, as can be seen in Figure 6A. The true stress σ_t from tensile test with smooth round bar specimen is expressed as

$$\begin{aligned}\sigma_t&=\int_0^a 2\pi r\sigma_{zz}dr/\pi r^2\\&=\sigma_{eq}[(1+2R/a){\cdot}\ln(1+a/2R)]\end{aligned} \tag{44}$$

Now, the Bridgman correction factor $\zeta_{Bridgman}$ can be written as

$$\zeta_{Bridgman}=\frac{\sigma_t}{\sigma_{eq}}=(1+2R/a){\cdot}\ln(1+a/2R) \tag{45}$$

According to Equation (45), after diffuse necking, the true stress obtained from a smooth round bar specimen can be corrected back to the corresponding equivalent stress. For the application of Equation (45), the instantaneous necking curvature radius R should be measured. It is very difficult to perform the measurement since the neck position is random in a smooth specimen, and it is practically impossible to be predetermined. Meanwhile, the neck region is usually smooth, and the radial linear

variable displacement transducer (LVDT) is not able to be positioned exactly. For this concern, Le Roy[44] has presented an empirical relation with a/R and the equivalent strain:

$$a/R = 1.1(\varepsilon_{eq} - \varepsilon_{p_{max}}) \tag{46}$$

Many researchers applied the Bridgman correction method and found that it is not accurate when the strain is large. Murata et al[45] performed numerical tensile tests with smooth round bar specimens and predefined flow stress–strain curves by Swift and Voce laws. The average stress obtained from the virtual tests was corrected with the Bridgman correction method. They found that the flow stress corrected by the Bridgman method overestimated the reference flow stress. In addition, they performed actual tensile test with a low carbon steel SS400 (in JIS). The average stress were corrected by an inverse method and the Bridgman method. Results showed that the Bridgman correction method yielded a higher flow stress than that of the inverse method they proposed. Similarly, La Rosa et al [46] conducted actual tensile tests of a D98 steel with flow stress obtained by the Bridgman method. The obtained flow stress–strain curve was treated as reference and then input for numerical tensile test. The average true stress from numerical modelling was then corrected by the Bridgman method and compared with the input flow stress. As can be seen in Figure 7, error between the input flow stress and the Bridgman corrected flow stress occurred when the equivalent strain was large. The error increased up to 10% when the strain was around 1.35.

It can be generally concluded that the Bridgman correction is not very accurate at large strain. The errors are mainly attributed to the assumption that the equivalent stress and equivalent strain are uniform over the specimen minimum cross section. Numerical analyses showed that the stress, strain, and stress triaxiality distribution over the specimen minimum cross-section differed from the Bridgman analytical solution.[38,47,48] Alves and Jones[36] performed tensile tests with axisymmetric notched specimens numerically, and they compared the strain distribution over the minimum cross section at fracture strain. Figure 8 shows the strain distribution for specimen with the initial geometry d_0=6.98mm and R=2mm at a fracture strain ε_f=0.55. It can be seen that the equivalent strain calculated by Equation (15) (referred as Bridgman in Figure 8) differs significantly with the numerical predictions (shown in red). In addition, close to the outer surface at the notch root, the strains in the radial and circumferential directions are not equal. Figure 9 shows the stress triaxiality evolution at the cross-section centre (r=0) and the notch root (r=a). The stress triaxiality at r=0 is calculated with the specimen initial geometric parameters while it is always 1/3 at the notch root, according to the Bridgman solution. It can be seen that the stress triaxiality at r=0 and r=a from numerical analysis shows considerable difference with the Bridgman solution. Bai et al[49] also studied the stress triaxiality at the minimum cross-section centre of notched round bar specimen and found that the stress triaxiality from numerical analysis (marked as Abaqus in Figure 10) differed significantly with the Bridgman solution; see Figure 10. The Bridgman correction method is not strictly accurate at large strains; however, it is still widely applied in large strain analysis.

In addition to the formula proposed by Bridgman, several similar analytical solutions can be found in the literature. The main difference for the derivation of these correction formulae is the determination of ρ. What is very interesting is that the first correction formula was proposed by Siebel shortly after the Second World

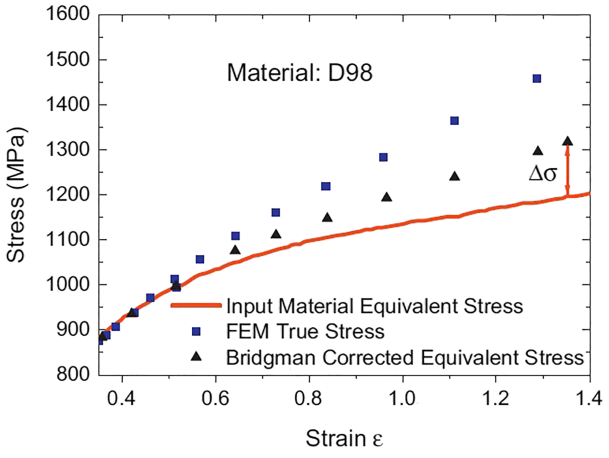

FIGURE 7 Comparison between input material equivalent stress and the Bridgman method corrected stress.[46] Finite element method (FEM) true stress is calculated by Equation (5) [Colour figure can be viewed at wileyonlinelibrary.com]

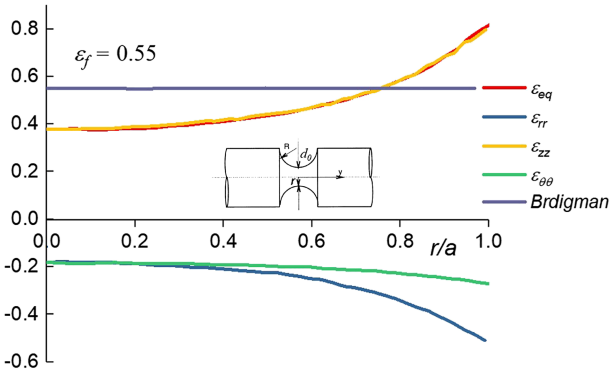

FIGURE 8 Strain distribution over an axisymmetric notched specimen (d_0=6.98mm and R=2mm) at the fracture strain[36] ε_f=0.55 [Colour figure can be viewed at wileyonlinelibrary.com]

War.[19] The distribution of Siebel solution was restricted since it was published in Germany. In Siebel work, ρ took the form

$$\rho = R(a/r)^n \tag{47}$$

Following the derivation process of the Bridgman method, Siebel correction formula can be written as

$$\zeta_{Siebel} = 1 + \frac{a}{(n+3)R} \tag{48}$$

Davidenkov[20] assumed that ρ is inversely proportional to r and can be given in the following form:

$$\rho = Ra/r \tag{49}$$

Correspondingly, the correction formula can be obtained and written as

$$\zeta_{D-S} = 1 + \frac{a}{4R} \tag{50}$$

It can be seen that when n=1, Equations (48) and (50) take the same form. Recently, another correction formula was proposed by Gromada et al.[43] It has the form

$$\zeta_G = 1 + \frac{a}{4R} + \frac{a(1-\beta)\alpha}{4R(4-\alpha)} \tag{51}$$

Gromada et al presented that when α=0.5 and β=0.5, Equation (51) can lead to more accurate results.

So far, several classical analytical formulae for correcting the average true stress obtained from smooth round bar specimen are briefly introduced. More details for the derivation of these formulae can be referred to Gromada et al.[43] Though these formulae have existed for a long time, the accuracy for applying each formula to a given material is not clear. As a result, selection of certain formula is somewhat arbitrary. For a better understanding of the accuracy of these classical correction formulae, Gromada et al[43] performed virtual tensile tests with smooth round bar specimens. In the numerical analyses, three models for flow stress–strain curve were applied: ideal plastic material, linear hardening material, and non-linear hardening material. The neck profile was captured in the numerical analyses, and the neck curvature radius R was fitted successively with the deformation. The average true stress were then corrected by the formulae introduced above. The error between the corrected flow stress and the input flow stress was normalized by the input flow stress and reproduced in Figure 11. It can be seen that these formulae are not accurate for the ideal plastic material. Especially for the Bridgman formula, the relative error reaches up to 10%. For the linear and non-linear hardening models,

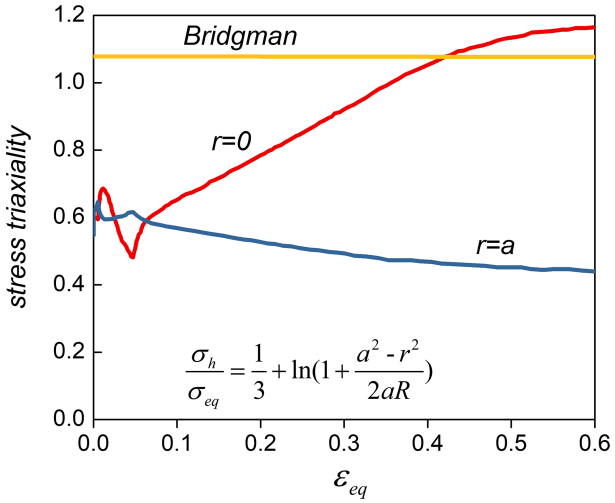

FIGURE 9 Stress triaxiality evolution at the cross-section centre (r=0) and the notch root (r=a) of an axisymmetric notched specimen with d_0=6.98mm and R=2mm.[36] The stress triaxiality at the cross-section centre was calculated with the initial geometric parameters [Colour figure can be viewed at wileyonlinelibrary.com]

the relative errors are acceptable and within 5%. It can also be observed that for the hardening rules considered, the Bridgman formula yields the highest relative errors. The Bridgman formula is not the most accurate one, though it is widely applied in practice. Since materials display different hardening behaviour, the accuracy of the above-mentioned correction formulae for a certain material is still not clear. Attention should be paid when these formulae are applied to derive the strain hardening in the post-necking regime for large strain analyses.

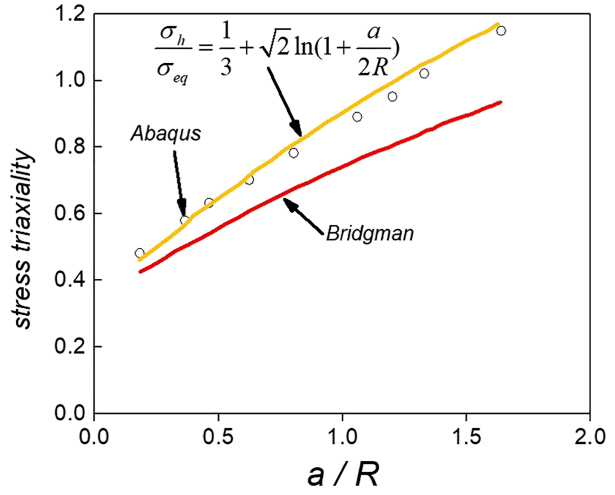

FIGURE 10 Stress triaxiality evolution evolution at the cross-section centre as a function of notch geometry by Bridgman solution and from numerical analysis[49] [Colour figure can be viewed at wileyonlinelibrary.com]

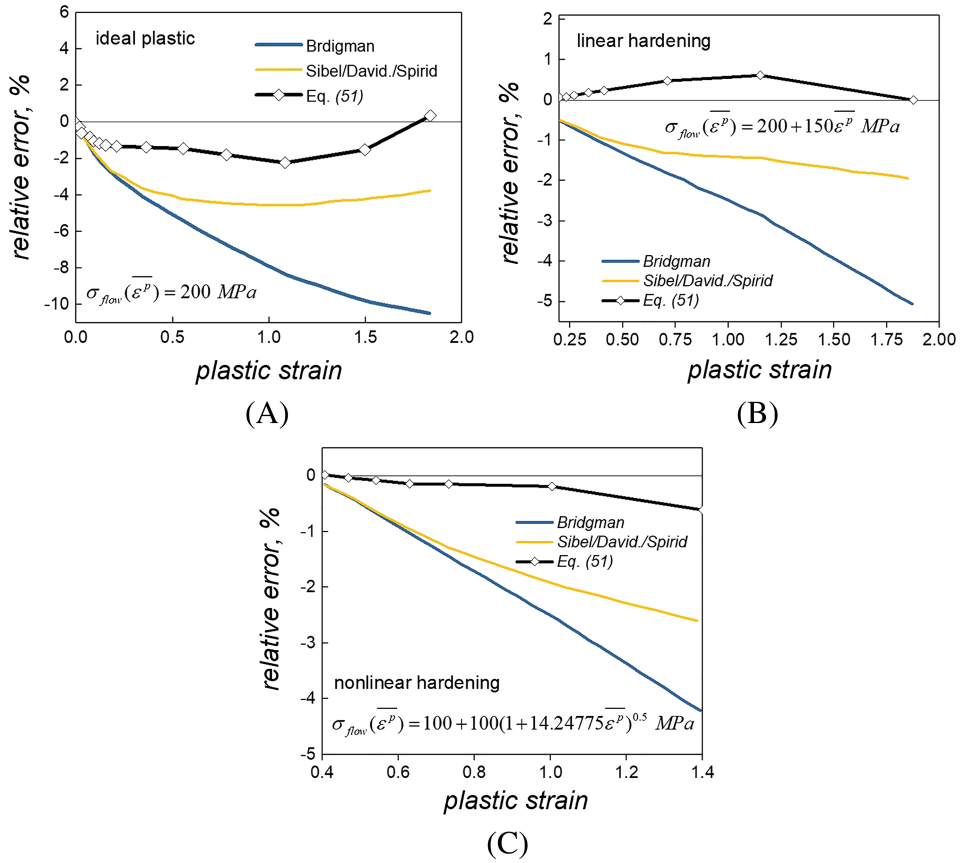

FIGURE 11 Relative errors following from the application of the correction formulae with different hardening rules: A, ideal plastic; B, linear hardening; and C, non-linear hardening[43] [Colour figure can be viewed at wileyonlinelibrary.com]

3.2 | Experimental-numerical iterative methods

Though there are several analytical solutions for the post-necking strain hardening identification with smooth round bar specimens, no one is suitable for flat specimens. For some thin sections, flat specimens are more favourable in practice. For this concern, many researchers applied a so-called experimental-numerical iterative method to retrieve the post-necking strain hardening behaviour. This method can be applied with both smooth round bar specimens and flat specimens since it iteratively adjusts the initially assumed post-necking strain hardening behaviour by minimizing the difference between certain measured and predicted physical quantities such as whole-field strains of the necking region,[21] total work (real or virtual) within the gauge section,[22-25] or the total axial force at a given displacement increment step[50-53] beyond the force maximum. Total axial force-elongation curve from a tensile test can be easily obtained, as well in numerical analysis. Zhano and Li[51] performed tensile tests experimentally and numerically of a No. 45 steel to obtain the material's strain hardening behaviour after diffuse necking, by controlling the difference of the total axial force within a given limit at each strain increment. Dunand and Mohr[50] proposed to use piece-wise linear relationship between the stress and the strain to represent the strain hardening behaviour in the post-necking regime. The hardening modulus of each piece is derived by minimizing the difference of the measured and computed load-displacement curve from smooth round bar tensile tests or major principal strain-force curve from a punch test. With the widespread availability of DIC, it is now not a difficult task to measure the strains within the neck. Wang and Tong[21] applied a multilinear hardening model to reproduce the hardening behaviour after diffuse necking. Based on the minimization of the discrepancy between the internal and external work in the necking zone during a tensile test, Coppoeters et al[23,24] presented a combined theoretical/experimental method to quantify post-necking strain hardening of ductile sheet materials.

For all these experimental-numerical iterative methods, one should assume the post-necking strain hardening rule beforehand for numerical modelling. There are several ways to depict the assumed post-necking hardening behaviour. The classical flow stress–strain models can be used alone or in combination. Coppoeters et al[23] selected the Swift and the Voce law to represent the strain hardening after diffuse necking.

The parameters of the Swift and Voce law were determined by minimizing the internal and external work in the necking zone of flat specimens. Kim et al[25] identified the parameters of the Swift and modified Voce laws with a virtual field method (VFM) method. Ling[53] proposed to use a linear and a power law together to represent post-necking strain hardening. A weight parameter w was iteratively determined when good agreement between the experimental measured and the numerical calculated force-extension curves was achieved. Defaisse et al[41] combined two Voce and a linear hardening laws to obtain flow stress–strain curve of a ultra high strength steel with round bar specimens. The parameters were fitted by minimizing the difference between the experimental measured and the numerically calculated load-minimum cross-section area reduction. In addition to define the hardening behaviour with classical models, one may choose multipiece linear relationship between the equivalent stress and equivalent strain. Dunand and Mohr[50] used four segments of linear hardening to present the constitutive law of a TRIP 780 steel after diffuse necking. The slope of each segment was determined by comparing the force-displacement curves from test and from numerical analyses with flat specimens. Marth et al[54] also applied several linear hardening laws to obtain the pre-necking and post-necking constitutive relation. An attempt using similar piecewise linear hardening model is also performed by Kajberg and Lindkvist.[55]

For the experimental-numerical iterative method, the accuracy of flow stress curves depends on the selected work hardening model. Complicated hardening model can be used for a specific material; however, more iterations are required for parameters calibration. Similarly, the more pieces defined to present the constitutive law, the higher cost of iteration for fulfilling the convergencecriteria. For the numerical analysis when using the experimental-numerical iterative method, usually the von Mises yielding criteria is applied. It was point out that triaxial stress state at the necking region and the yield function may influence the flow stress–strain curve at large strains.[56,57] Especially, the numerical analyses does not take the damage evolution into account, since ductile fracture is widely acknowledged as void nucleation, growth, and coalescence. However, discussions on the effects of triaxial stress state at the necking region and the yield function on the flow stress–strain curves are very limited, and more attentions can be paid for this concern.

3.3 | Inverse methods

In addition to the analytical methods and the experimental-numerical iteration method, some researchers identified the post-necking hardening with a so-called inverse method. This method usually works in this way: (a) perform numerical modelling with tensile specimens with predefined equivalent stress–strain curve; (b) identify suitable approach to define the minimum cross-section area for equivalent strain characterization after diffuse necking; (c) investigate the relationship between the true stress from numerical modelling and the input equivalent stress at the same equivalent strain; and (d) search for a formula to fit the relation and used as a correction function. Zhang et al[26-28] applied this strategy to obtain true stress–strain curve from flat specimens with different aspect ratios, for homogeneous and inhomogeneous materials. In addition, Zhang et al also proposed to use axisymmetric notched bar to identify true stress–strain curve in large strains.[42] The true stress–strain curve from a notched bar specimen can be converted to that from a smooth round bar specimen. However, for Zhang's methods, what one derived is the true stress–strain curve, instead of the equivalent stress–strain curve. The true stress–strain curve should be further corrected with other methods, such as Bridgman correction method. Scheider et al[58] performed tensile tests with flat specimens numerically and proposed a factor for equivalent stress correction after diffuse necking. A power law with hardening exponents of n=5, 7, 10, and 20 were assumed to present the strain hardening behaviour. The factor proposed by Scheider includes not only the effect of stress triaxiality on the stress state but also the conversion of the so-called "nominal" area (expressed as$w^2(t_0/w_0)$, w is the instant specimen width) to the actual area of the minimum cross section after the maximum tensile load. The correction factor is a function of the equivalent strain (ε_{eq}) and the strain at diffuse necking (ε_u) (Equation 52). It should be noted that this correction factor is only valid for thickness reduction ($\Delta t/t_0$) up to 55% and suitable for flat specimens with aspect ratio w_0/t_0=4.

$$\sigma_{eq}(\varepsilon_{eq}) = \begin{cases} Pw_0/(t_0 b^2) & \varepsilon_{eq} \le 1.42\varepsilon_u \\ Pw_0/(t_0 b^2)\left[0.22(\varepsilon_{eq} - 1.42\varepsilon_u)(\varepsilon_{eq} - 0.78) + 1\right] & \varepsilon_{eq} > 1.42\varepsilon_u \end{cases} \quad (52)$$

Choung and Cho[59] also attempted to identify the strain hardening behaviour after diffuse necking with flat specimens. The aspect ratio of flat specimens ranged from 1 to 10 and the power-law model (Equation 28) with hardening exponent from 0.1 to 0.3 were assumed. By comparing the average true stress from numerical tensile test and the input flow stress, they proposed the following correction formula:

$$\zeta_{Choung}(\overline{\varepsilon^p}) = \begin{cases} 1 & \overline{\varepsilon^p} \le 1.4\varepsilon_u \\ \alpha\overline{\varepsilon^p}^2 + \beta\overline{\varepsilon^p} + \gamma & \overline{\varepsilon^p} > 1.4\varepsilon_u \end{cases} \tag{53}$$

$$\begin{aligned} \alpha &= -0.0704n - 0.0275 \\ \beta &= 0.455n - 0.2926 \\ \gamma &= 0.1592n + 1.024 \end{aligned} \tag{54}$$

They stated that the strain when diffuse necking took place (at the same time the force maximum is achieved) is approximately equal to the hardening exponent applied, namely, $\varepsilon_u \approx n$. Same results can be found in Zhang's work via plastic instability analysis of axisymmetric notch round bar specimens.[42] It should be noted that in Choung's work, the minimum cross-section area should be measured manually in actual tests, which is a strong challenge indeed. From both Scheider's and Choung's work, it can be found that when the equivalent strain or the equivalent plastic strain is smaller than 1.4 time of ε_u, the average true stress does not necessary to be corrected. This also means that the Bridgman assumption are only valid shortly after diffuse necking.

Initiated from Zhang's work[42] and considering the advantages of axisymmetric notch round bar specimen, Tu et al identified an axisymmetric notched bar with specific notch geometry a_0/R_0=2.[60] With a single correction factor G^m, the average true stress from the notched specimen can be converted to the material's equivalent stress–strain curve; see Equation (55). The correction factor G^m was further expressed as a function of the materials' hardening exponent, which was approximately equal to the strain at diffuse necking, ε_u. Figure 12 shows the "magic" notch and the relation between the correction factor G^m and ε_u. Numerical analysis indicated that the notch geometry parameter a/R is almost constant after the force maximum. The axisymmetric notch round bar specimen with a_0/R_0=2 is therefore called "magic" notch.

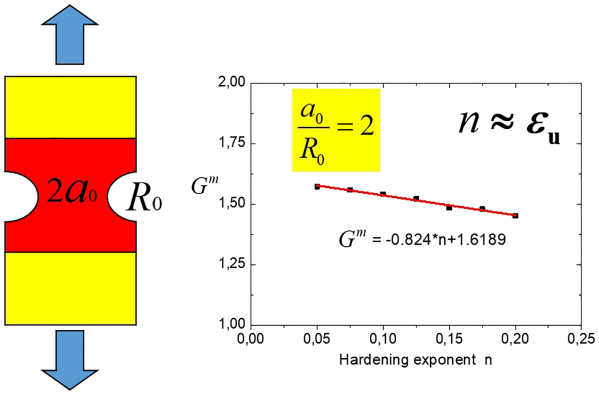

FIGURE 12 A "magic" axisymmetric notched specimen for flow stress–strain curve identification in large strains with a single correction factor. The correction factor is a linear function of the hardening exponent n, which can be obtained as the strain corresponding to the force maximum (diffuse necking initiates) [60] [Colour figure can be viewed at wileyonlinelibrary.com]

$$\sigma_{eq} = \frac{P}{AG^m} \tag{55}$$

In addition to the "magic" notch, Tu et al proposed a correction formula, with which the average true stress from axisymmetric notched specimens with "any" notch geometry a_0/R_0 can be converted to materials' equivalent stress–strain curve.[61,62] The correction formula is a function of the deformation ε_{eq}, the notch geometry a_0/R_0 and material's hardening exponent n. This correction formula works not only for the hardening materials but also for the perfectly plastic materials; see Figure 13. It is well

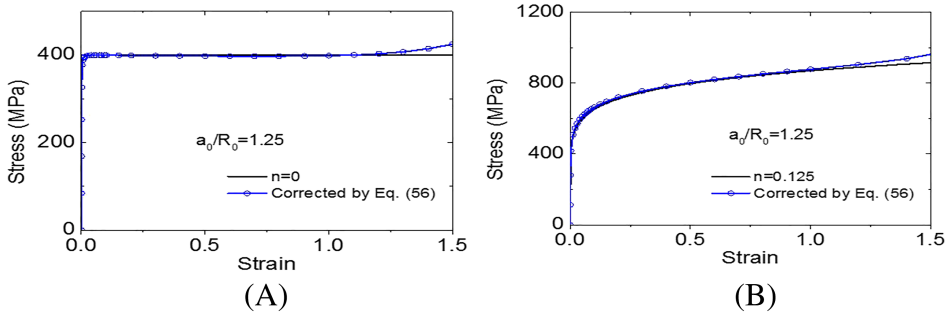

FIGURE 13 Verification of the correction formulae Equation (56) with A, perfectly plastic material and B, power-law hardening material.[61] The equivalent stress–strain curves were converted from flow stress–strain curves which were constructed by Equation (28) [Colour figure can be viewed at wileyonlinelibrary.com]

known that the fracture strain strongly depends on the stress triaxiality, which is defined by the ratio of hydrostatic stress and von Mises equivalent stress.[40,63-66] Fracture strain decreases with the increase of stress triaxiality when stress triaxiality is larger than 1/3. For axisymmetric notched tensile specimen, the stress triaxiality is a function of notch geometry a_0/R_0 and larger than 1/3. Larger a_0/R_0 corresponds to a higher stress triaxiality, therefore, resulting in a smaller failure strain. For the application of Tu's correction function in measuring equivalent stress–strain curve at large strains, it is therefore not recommended to use specimens with very large a_0/R_0.

$$\begin{aligned} \xi &= f(n)\cdot(b_{1,n=0}\cdot\varepsilon_{eq} + b_{2,n=0}) \\ f(n) &= -0.22942\cdot n^2 - 0.36902\cdot n + 1 \\ b_{1,n=0} &= 0.03232(a_0/R_0)^2 - 0.27(a_0/R_0) + 0.3688 \\ b_{2,n=0} &= -0.04084(a_0/R_0)^2 + 0.3557(a_0/R_0) + 1.0577 \end{aligned} \tag{56}$$

For the inverse methods, the correction factor and formulae were derived with numerical tensile modelling and a preselected strain hardening constitutive is assumed. Since each material exhibits a specific hardening rule, one cannot guarantee the accuracy for the application of the correction factors proposed in the inverse way. One have to search a suitable method to verify the obtained hardening behaviour, for example, running numerical modelling in parallel and compare the load-elongation curves from the experiments and the numerical modelling.

4 | CONCLUSIONS

In this paper, the standard tensile tests and the methods for post-necking strain hardening characterization are reviewed. Based on the analysis and discussions, the main findings are summarized as follows:

1. Post-necking strain hardening behaviour characterization is an important issue for modelling problems when large strains are involved; however, it is still a strong challenge since the availability and accuracy of the proposed methods are not clearly demonstrated. Each material exhibits a specific hardening rule. Different approximate approaches to the same problem might deliver good hints for someone finally getting the exact solution, sooner or later.
2. The analytic correction formulae are only suitable for smooth round bar specimens and fail to provide accurate results for the perfectly plastic materials. For hardening materials, the analytical methods provide acceptable results. However, attentions should be paid since both the triaxiality and yield surface will influence the strain hardening in the necking zone. Though the Bridgman correction formula is widely used, it is not the most accurate one among the analytical methods.
3. The experimental-numerical iterative method yields trustful strain hardening behaviour in the post-necking regime. The convergence efficiency depends significantly on the pre-assumed constitutive law. Multiple linear piecewise hardening is a good choice; however, the iterative cost increases rapidly when the segments increase.
4. The inverse method is straightforward and easy to use in practice. However, since the correction formula proposed in an inverse way is based on a predefined hardening rules, the accuracy is a controversial issue for an actual material. It is necessary to verify the obtained strain hardening in an cost-effective way.

ACKNOWLEDGEMENT

The authors greatly acknowledge the Chinese Scholarship Council and the Research Council of Norway (PETROMAKS2 Programme, SMACC project 228513) for funding support through the PETROMAKS2 Programme, Contract No. 228513/E30.

ORCID

Zhiliang Zhang https://orcid.org/0000-0002-9557-3455

REFERENCES

1. Trana K. Finite element simulation of the tube hydroforming process—bending, preforming and hydroforming. *J Mater Process Technol*. 2002;127(3):401-408.
2. Aue-U-Lan Y, Ngaile G, Altan T. Optimizing tube hydroforming using process simulation and experimental verification. *Int J Mater Prod Technol*. 2004;146(1):137-143.
3. Padmanabhan R, Oliveira MC, Alves JL, Menezes LF. Influence of process parameters on the deep drawing of stainless steel. *Finite Elem Anal Des*. 2007;43(14):1062-1067.
4. Yoshihara S, Manabe K, Nishimura H. Effect of blank holder force control in deep-drawing process of magnesium alloy sheet. *J Mater Process Technol*. 2005;170(3):579-585.
5. Choi Y, Heo Y, Kim HY, Seo D. Investigations of weld-line movements for the deep drawing process of tailor welded blanks. *J Mater Process Technol*. 2000;108(1):1-7.
6. Bagherzadeh S, Mirnia MJ, Dariani BM. Numerical and experimental investigations of hydro-mechanical deep drawing process of laminated aluminum/steel sheets. *J Manuf Process*. 2015;18:131-140.

7. Wang N-M, Budiansky B. Analysis of sheet metal stamping by a finite-element method. *J Appl Mech*. 1978;45(1):73-82.
8. Hu P, Shi D, Ying L, Shen G, Liu W. The finite element analysis of ductile damage during hot stamping of 22MnB5 steel. *Mater Des*. 2015;69:141-152.
9. Wang A, Liu J, Gao H, Wang L-L, Masen M. Hot stamping of AA6082 tailor welded blanks: experiments and knowledge-based cloud–finite element (KBC-FE) simulation. *J Mater Process Technol*. 2017;250:228-238.
10. Tu S, Ren X, He J, Zhang Z. Numerical study on the effect of the Lüders plateau on the ductile crack growth resistance of SENT specimens. *Int J Fract*. 2018;214(2):185-200.
11. Shuai J, Tu S, Wang J, Ren X, He J, Zhang Z. Determining critical CTOA from energy-load curves with DWTT specimen. *Eng Fract Mech*. 2017;186:47-58.
12. Han K, Shuai J, Deng X, Kong L, Zhao X, Sutton M. The effect of constraint on CTOD fracture toughness of API X65 steel. *Eng Fract Mech*. 2014;124:167-181.
13. Zhang ZL, Thaulow C, Ødegård J. A complete Gurson model approach for ductile fracture. *Eng Fract Mech*. 2000;67(2):155-168.
14. Zhang ZL, Hauge M, Thaulow C. Two-parameter characterization of the near-tip stress fields for a bi-material elastic-plastic interface crack. *Int J Fract*. 1996;79(1):65-83.
15. Xu J, Zhang ZL, Østby E, Nyhus B, Sun DB. Constraint effect on the ductile crack growth resistance of circumferentially cracked pipes. *Eng Fract Mech*. 2010;77(4):671-684.
16. Xu J, Zhang ZL, Østby E, Nyhus B, Sun DB. Effects of crack depth and specimen size on ductile crack growth of SENT and SENB specimens for fracture mechanics evaluation of pipeline steels. *Int J Press Vessels Pip*. 2009;86(12):787-797.
17. Ren XB, Zhang ZL, Nyhus B. Effect of residual stresses on the crack-tip constraint in a modified boundary layer model. *Int J Solids Struct*. 2009;46(13):2629-2641.
18. Bridgman PW. *Studies in Large Plastic Flow and Fracture*, Vol. 177. New York: McGraw-Hill; 1952.
19. Siebel E, Schwaigere S. Mechanics of tensile test. *Arch Eisenhuttenwes*. 1948;19:145-152.
20. Davidenkov WW. Mechanical methods of testing analysis of the state of stress in the neck of a tension specimen. In: Proc. ASTM; 1946.
21. Wang L, Tong W. Identification of post-necking strain hardening behavior of thin sheet metals from image-based surface strain data in uniaxial tension tests. *Int J Solids Struct*. 2015;75:12-31.
22. Coppieters S, Sumita S, Yanaga D, Denys K, Debruyne D, Kuwabara T. Identification of post-necking strain hardening behavior of pure titanium sheet. *Residual Stress, Thermomechanics & Infrared Imaging, Hybrid Techniques and Inverse Problems*; 2016:59-64.
23. Coppieters S, Cooreman S, Sol H, Van Houtte P, Debruyne D. Identification of the post-necking hardening behaviour of sheet metal by comparison of the internal and external work in the necking zone. *J Mater Process Technol*. 2011;211(3):545-552.
24. Coppieters S, Kuwabara T. Identification of post-necking hardening phenomena in ductile sheet metal. *Exp Mech*. 2014;54(8):1355-1371.
25. Kim J-H, Serpantié A, Barlat F, Pierron F, Lee M-G. Characterization of the post-necking strain hardening behavior using the virtual fields method. *Int J Solids Struct*. 2013;50(24):3829-3842.
26. Zhang ZL, Hauge M, Ødegård J, Thaulow C. Determining material true stress–strain curve from tensile specimens with rectangular cross-section. *Int J Solids Struct*. 1999;36(23):3497-3516.
27. Zhang ZL, Ødegård J, Søvik OP. Determining true stress–strain curve for isotropic and anisotropic materials with rectangular tensile bars: method and verifications. *Comput Mater Sci*. 2001;20(1):77-85.
28. Yuan WJ, Zhang ZL, Su YJ, Qiao LJ, Chu WY. Influence of specimen thickness with rectangular cross-section on the tensile properties of structural steels. *Mater Sci Eng A*. 2012;532:601-605.
29. ASTM I. ASTM E8/E8M-16a: standard test methods for tension testing of metallic materials. West Conshohocken, PA, USA: ASTM International; 2016.
30. Aegerter J, Kühn H-J, Frenz H, Weißmüller C. EN ISO 6892-1: 2009 tensile testing: initial experience from the practical implementation of the new standard. *Mater Test*. 2011;53(10):595-603.
31. 6892-2 ISO. Metallic materials—tensile testing: Part; 2011.
32. JIS Z2241. Metallic materials tensile testing method of test at room temperature; 2011.
33. Yasnikov IS, Vinogradov A, Estrin Y. Revisiting the Considère criterion from the viewpoint of dislocation theory fundamentals. *Scr Mater*. 2014;76:37-40.
34. Peng J, Wu PD, Huang Y, et al. Effects of superimposed hydrostatic pressure on fracture in round bars under tension. *Int J Solids Struct*. 2009;46(20):3741-3749.
35. Kao AS, Kuhn HA, Richmond O, Spitzig WA. Tensile fracture and fractographic analysis of 1045 spheroidized steel under hydrostatic pressure. *J Mater Res*. 1990;5(1):83-91.
36. Alves M, Jones N. Influence of hydrostatic stress on failure of axisymmetric notched specimens. *J Mech Phys Solids*. 1999;47(3):643-667.
37. Hollomon JH. Tensile deformation. *Aime Trans*. 1945;12(4):1-22.
38. Mirone G, Corallo D. A local viewpoint for evaluating the influence of stress triaxiality and lode angle on ductile failure and hardening. *Int J Plast*. 2010;26(3):348-371.
39. Ramberg W, Osgood WR. Description of stress-strain curves by three parameters; 1943.
40. Tu S, Ren X, Kristensen TA, He J, Zhang Z. Study of low-temperature effect on the fracture locus of a 420-mpa structural steel with the edge tracing method. *Fatigue Fract Eng Mater Struct*. 2018;41(8):1649-1661.
41. Defaisse C, Mazière M, Marcin L, Besson J. Ductile fracture of an ultra-high strength steel under low to moderate stress triaxiality. *Eng Fract Mech*. 2018;194:301-318.
42. Zhang ZL, Hauge M, Thaulow C, Ødegård J. A notched cross weld tensile testing method for determining true stress–strain curves for weldments. *Eng Fract Mech*. 2002;69(3):353-366.
43. Gromada M, Mishuris G, Öchsner A. *Correction Formulae for the Stress Distribution in Round Tensile Specimens at Neck Presence*. Springer Science & Business Media; 2011.
44. Le Roy G, Embury JD, Edwards G, Ashby MF. A model of ductile fracture based on the nucleation and growth of voids. *Acta Metall*. 1981;29(8):1509-1522.

45. Murata M, Yoshida Y, Nishiwaki T. Stress correction method for flow stress identification by tensile test using notched round bar. *J Mater Process Technol*. 2018;251:65-72.
46. La Rosa G, Risitano A, Mirone G. Postnecking elastoplastic characterization: degree of approximation in the Bridgman method and properties of the flow-stress/true-stress ratio. *Metall Mater Trans A*. 2003;34(3):615-624.
47. Hancock JW, Brown DK. On the role of strain and stress state in ductile failure. *J Mech Phys Solids*. 1983;31(1):1-24.
48. Mirone G. A new model for the elastoplastic characterization and the stress–strain determination on the necking section of a tensile specimen. *Int J Solids Struct*. 2004;41(13):3545-3564.
49. Bai Y, Teng X, Wierzbicki T. On the application of stress triaxiality formula for plane strain fracture testing. *J Eng Mater Technol*. 2009;131(2):021002.
50. Dunand M, Mohr D. On the predictive capabilities of the shear modified gurson and the modified Mohr–Coulomb fracture models over a wide range of stress triaxialities and lode angles. *J Mech Phys Solids*. 2011;59(7):1374-1394.
51. Zhano KS, Li ZH. Numerical analysis of the stress-strain curve and fracture initiation for ductile material. *Eng Fract Mech*. 1994;49(2):235-241.
52. Zhao K, Wang L, Chang Y, Yan J. Identification of post-necking stress–strain curve for sheet metals by inverse method. *Mech Mater*. 2016;92:107-118.
53. Ling Y. Uniaxial true stress-strain after necking. *AMP J Technol*. 1996;5(1):37-48.
54. Marth S, Häggblad H, Oldenburg M, Östlund R. Post necking characterisation for sheet metal materials using full field measurement. *J Mater Process Technol*. 2016;238:315-324.
55. Kajberg J, Lindkvist G. Characterisation of materials subjected to large strains by inverse modelling based on in-plane displacement fields. *Int J Solids Struct*. 2004;41(13):3439-3459.
56. Dunand M, Mohr D. Hybrid experimental–numerical analysis of basic ductile fracture experiments for sheet metals. *Int J Solids Struct*. 2010;47(9):1130-1143.
57. Tardif N, Kyriakides S. Determination of anisotropy and material hardening for aluminum sheet metal. *Int J Solids Struct*. 2012;49(25):3496-3506.
58. Scheider I, Brocks W, Cornec A. Procedure for the determination of true stress-strain curves from tensile tests with rectangular cross-section specimens. *J Eng Mater Technol*. 2004;126(1):70-76.
59. Choung JM, Cho SR. Study on true stress correction from tensile tests. *J Mech Sci Technol*. 2008;22(6):1039-1051.
60. Tu S, Ren X, Nyhus B, Akselsen OM, He J, Zhang Z. A special notched tensile specimen to determine the flow stress-strain curve of hardening materials without applying the Bridgman correction. *Eng Fract Mech*. 2017;179:225-239.
61. Tu S, Ren X, He J, Zhang Z. A method for determining material's equivalent stress-strain curve with any axisymmetric notched tensile specimens without Bridgman correction. *Int J Mech Sci*. 2018;135:656-667.
62. Tu S, Ren X, He J, Zhang Z. Experimental measurement of temperature-dependent equivalent stress-strain curves of a 420 MPa structural steel with axisymmetric notched tensile specimens. *Eng Fail Anal*. 2019;100:312-321.
63. Børvik T, Hopperstad OS, Berstad T. On the influence of stress triaxiality and strain rate on the behaviour of a structural steel. Part II. Numerical study. *Eur J Mech A Solids*. 2003;22(1):15-32.
64. Børvik T, Hopperstad OS, Dey S, Pizzinato EV, Langseth M, Albertini C. Strength and ductility of Weldox 460 E steel at high strain rates, elevated temperatures and various stress triaxialities. *Eng Fract Mech*. 2005;72(7):1071-1087.
65. Hopperstad OS, Børvik T, Langseth M, Labibes K, Albertini C. On the influence of stress triaxiality and strain rate on the behaviour of a structural steel. Part I. Experiments. *Eur J Mech A Solids*. 2003;22(1):1-13.
66. Zhang ZL, Niemi E. Studies on the ductility predictions by different local failure criteria. *Eng Fract Mech*. 1994;48(4):529-540.

How to cite this article: Tu S, Ren X, He J, Zhang Z. Stress–strain curves of metallic materials and post-necking strain hardening characterization: A review. *Fatigue Fract Eng Mater Struct*. 2019;1–17. https://doi.org/10.1111/ffe.13134